IET Research Journals

Scaling laws for electrodynamic suspension in high-speed transportation

ISSN 1751-8644
doi: 0000000000
www.ietdl.org

Michael Flankl[1], *Tobias Wellerdieck*[1], *Arda Tüysüz*[1], *Johann W. Kolar*[1]

[1] *Power Electronic Systems Laboratory, Swiss Federal Institute of Technology, Zurich, Switzerland*
* *E-mail: flankl@lem.ee.ethz.ch*

Abstract: Electrodynamic suspension (EDS) is based on the repulsive force created by induced eddy currents in a conductive body (rail), a magnetic excitation system and a relative speed between the magnet field and the rail. When the excitation system is realized as Halbach array of permanent magnets and mounted on a moving vehicle (pod), it can create the required lift to levitate the pod and no further mechanical suspension is needed. EDS is one of the few vehicle suspension concepts that could operate reliably at high speeds. Therefore, it gains interest for high-speed transportation applications as for the *Hyperloop* project, which is mainly driven by the Space Exploration Technologies Corporation (SpaceX). Electrodynamic fields and forces have been analysed in detail in literature; however, the sophistication and/or limited applicability of analytical approaches or the computational burden of FEM/numerical methods render those impractical for the initial design of EDS systems. Therefore, power and loss scaling laws for EDS systems are derived in this work. A 3D simulation for a design example shows that the scaling law is within 10% deviation. Finally, the drag coefficient of EDS systems are compared to other forms of commercial high-speed ground and air transportation systems. A pod with EDS running in vacuum has the potential of decreasing energy consumption significantly above the cruising speeds of modern subsonic airliners.

1 Introduction

Even though the concept of high-speed travel in tubes is a more-than-a-century-old idea [1], and concrete technical designs for high-speed ground transportation in (partially) evacuated tubes have been published already several decades ago [2], the idea has recently regained popularity [3–6]. Also Elon Musk's announcement in 2013 contributed to the regaining of interest, which details the design of the *Hyperloop* [7], a form of high-speed ground transportation that would reduce the travel time from Los Angeles to San Francisco ($563\ \mathrm{km}/350\ \mathrm{miles}$) down to 35 minutes. The proposed system is based on the idea of using small vehicles, denoted as pods that carry goods or passengers. The pods travel inside tubes, which are partially evacuated in order to eliminate or minimize air friction and it is intended to be an alternative for bullet trains up to distances of $1500\ \mathrm{km}/900\ \mathrm{miles}$ [7].

For maintaining a reliable operation at speeds above the state-of-the-art in ground transportation (up to $\approx 100\,\mathrm{m/s} = 360\,\mathrm{km/h}$ for high-speed trains), contactless methods are needed for the suspension of a vehicle. Two candidate technologies considered today are air bearings and magnetic levitation. Electrodynamic suspension (EDS) systems with permanent magnets (PMs) and passive secondaries fall within the latter category, and they offer an interesting solution due to their simple construction and control.

In such systems, PMs are usually arranged as linear Halbach arrays, in order to generate a strong magnetic field with a minimum weight [8]. When the PMs are in motion, e.g. mounted at the bottom of the suspended vehicle, facing an electrically conductive and non-ferromagnetic (otherwise an attractive force will counteract the levitation force) surface (henceforth called the secondary), eddy currents are induced in the secondary, which in turn lead to repulsive Lorentz forces; hence suspension.

A vast amount of literature analysing electrodynamic fields and forces has been published over the last decades. Knowles has developed a general theory of EDS systems using a double Fourier series approach in [10]; Hill has solved Maxwell's equations for obtaining lift and drag forces in simplified EDS geometries in [11]; and Ko and Ham have studied the transient behaviour of an EDS with a linear Halbach array using wavelet transformation in [12]. In addition to such analytical efforts, scholars have also commonly used finite element method (FEM) to analyse the performance of numerous EDS variants [13–15].

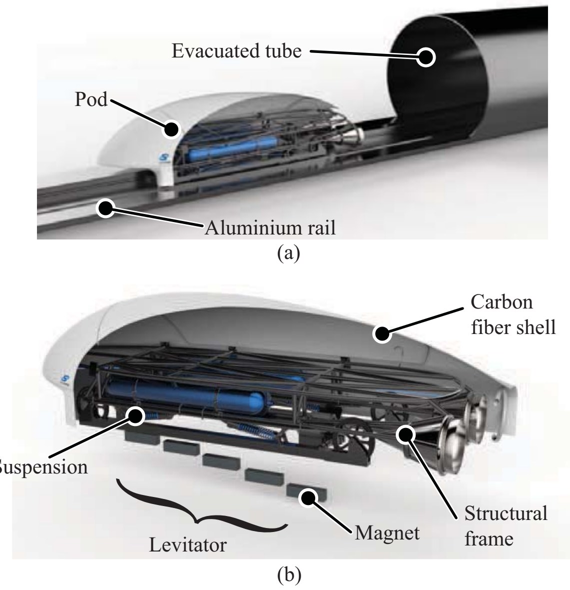

Fig. 1: (a) Schematic representation of a system for the *Hyperloop* student competition. (b) Pod, rail and the evacuated tube; detailed view of the pod (Images courtesy of *Swissloop [9]).*

However, the sophistication and/or limited applicability of analytical approaches or the computational burden of FEM/numerical methods render those impractical for the initial design of EDS systems, which motivates the development of scaling laws. In a recent work, Carlstedt *et. al.* provided an in-depth discussion about the use of dimensional analysis for deriving similarity relationships. However, the analysis is based on a single PM [16] and is not extended towards a realistic EDS system. On the other hand, [17] provides an analytic calculation and FEM simulations of forces in an EDS system, however, a statement on energy consumption, condensed in a scaling law, is not included.

Therefore, the contribution of this paper is towards the study of feasibility and limitations of utilizing EDS systems in high-speed transportation and deriving power and loss scaling laws therefore. The detailed modelling of the field source is excluded and the analysis starts with the assumption of a given magnetic field, which not only simplifies the derivation, but also broadens the analysis towards various EDS systems with different field sources. Both the lift and drag forces, as well as their ratio, which is the so-called drag coefficient, are derived analytically in Sec. 2. Afterwards, FEM simulations are used not only to validate analytical scaling laws, but also to quantify the effects occurring in practical designs in Sec. 3. Moreover, an example levitator design is shown in Sec. 4. Specifications for the application example are taken from the *Hyperloop* student competition organized by the Space Exploration Technologies Corporation *(SpaceX)*, where the participants are asked to design and build a scaled-down model of a pod and test it on an approximately 1 mile (1.6 km) long test track. The track comprises a tube that can be evacuated; two horizontal, flat, aluminium surfaces (rails), above which the pod can be suspended; and an aluminium beam, which can be used for guidance of the pod. Fig. 1 illustrates *Swissloop*, the pod designed by the students of ETH Zurich for this competition [9].

For evaluating the design example, a 3D simulation is conducted and results are compared to the derived scaling law. Finally, the drag coefficient of EDS systems are compared to other forms of state-of-the-art high-speed ground and air transportation in Sec. 5.

2 Scaling Laws: A Simple and General Representation of the EDS System

The key elements of any EDS system are a magnetic field and an electrically conductive body (secondary). Both are in relative motion with respect to each other with a slip speed of v_s, while the vehicle moves above the secondary with a speed of v_1. If the source of the magnetic field (primary) is a PM array or an electromagnet excited with a DC current, which is fixed on the vehicle, the reference system for the analysis is fixed to the secondary, and the slip speed equals the vehicle speed, $v_\mathrm{s} = v_1$. On the other hand, different EDS systems employing either rotating PM arrays [18–20] or single-sided linear induction machines [21, 22] have also been proposed in literature, in which case $v_\mathrm{s} \neq v_1$.

An analytical model for the magnetic field, induced current field and the resulting Lorentz force in the secondary is derived in the following. Even though a fixed PM array mounted on the vehicle is of primary interest, for the sake of generality, the slip speed v_s is used instead of the vehicle or primary speed v_1, and a magnetic field with a given form is assumed rather than conducting a detailed modelling of different primary arrangements. For brevity, both longitudinal end effects and transversal edge effects are omitted at the first step by assuming both the primary and secondary to be infinitely long and wide (cf. x-direction and y-direction in Fig. 2 respectively).

The analysis starts with the assumption of a sinusoidal flux density on the top side of the secondary with an amplitude of $\hat{B}$ and an x-axis spatial period of $2\,\tau$, with τ being the pole pitch. The flux density, which could be resulting from a Halbach arrangement of

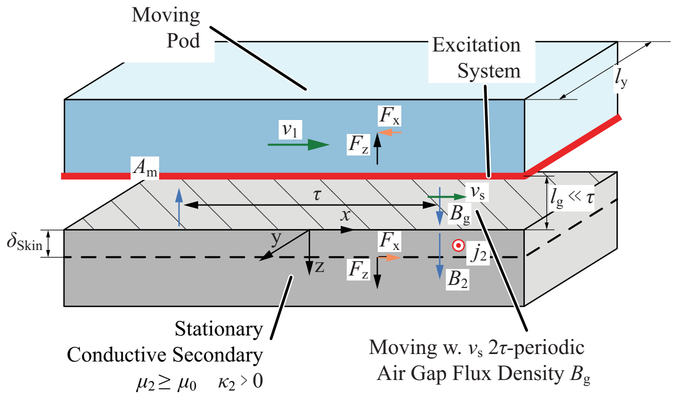

Fig. 2: Illustration of the fields, forces and currents in the EDS system.

magnets above the air gap, is described by the expression

$$\vec{B_\mathrm{g}}(t) = \begin{pmatrix} B_\mathrm{g,x} \\ B_\mathrm{g,y} \\ B_\mathrm{g,z} \end{pmatrix} = \begin{pmatrix} 0 \\ 0 \\ \hat{B}_\mathrm{g} \cdot \sin\left(\pi \, \frac{x}{\tau} + \omega_\mathrm{s} t\right) \end{pmatrix}, \tag{1}$$

where ω_s is the slip frequency, which is also the frequency of the eddy current density j_2 induced in the secondary

$$\omega_\mathrm{s} = \pi \, \frac{v_\mathrm{s}}{\tau} \, . \tag{2}$$

For obtaining the flux density distribution in the secondary $\vec{B_2}$, the following equations, which are derived from Ampere's law, the Maxwell-Faraday equation and Gauss's law for magnetism, are applied

$$\nabla \times (\nabla \times \vec{B_2}) = -\mu_2 \cdot \kappa_2 \cdot \frac{\partial \vec{B_2}}{\partial t} \, , \tag{3}$$

$$\frac{\partial B_\mathrm{2,x}}{\partial x} = -\frac{\partial B_\mathrm{2,z}}{\partial z} \, , \tag{4}$$

where μ_2 is the secondary permeability and κ_2 is the secondary conductivity. As outlined in [23], one can define the flux density in the secondary $\vec{B_2}$ as the real part of an exponential function with complex eigenvalue $\underline{\vec{s_\mathrm{B}}}$,

$$\underbrace{\begin{pmatrix} B_\mathrm{2,x}(t) \\ B_\mathrm{2,y}(t) \\ B_\mathrm{2,z}(t) \end{pmatrix}}_{=\vec{B_2}(t)} = \mathrm{Re}\left\{ \underline{\vec{B_2}} \cdot \exp\left(\underline{\vec{s_\mathrm{B}}}^{T} \cdot \begin{pmatrix} x \\ y \\ z \\ t \end{pmatrix} \right) \right\} . \tag{5}$$

With (4) and (5), one can obtain the solution for (3), where (1) is the boundary condition at the interface of air gap and secondary. With the qualified assumption that the pole pitch is sufficiently larger than the secondary skin depth

$$\tau \gg \delta_\mathrm{Skin} \, , \tag{6}$$

one can obtain the complex eigenvalue $\underline{\vec{s_\mathrm{B}}}$ of the field problem as

$$\underline{\vec{s_\mathrm{B}}} = \begin{pmatrix} \mathrm{j}\,{}^{\pi}/_{\tau} \\ 0 \\ -\,{}^{(1+\mathrm{j})}/_{\delta_\mathrm{Skin}} \\ \mathrm{j}\,\omega_\mathrm{s} \end{pmatrix}, \tag{7}$$

IET Research Journals, pp. 1–8

with the skin depth

$$\delta_{\mathrm{Skin}} = \sqrt{\frac{2}{|\omega_{\mathrm{s}}| \cdot \mu_2 \cdot \kappa_2}} = \sqrt{\frac{2 \cdot \tau}{\pi \cdot |v_{\mathrm{s}}| \cdot \mu_2 \cdot \kappa_2}} \,. \qquad (8)$$

Therefore, the amplitude of the field distribution in the secondary $\underline{\vec{B_2}}$ can be obtained as

$$\underline{\vec{B_2}} = \hat{B}_{\mathrm{g}} \cdot \begin{pmatrix} -\,{}^{(1+\mathrm{j})}/_{\delta_{\mathrm{Skin}}} \cdot {}^{\pi}/_{\tau} \\ 0 \\ -\mathrm{j} \end{pmatrix} \qquad (9)$$

and the solution for the secondary flux density can be expressed as a function of time as

$$\vec{B_2}(t) = \hat{B}_{\mathrm{g}} \cdot \exp\left(-\frac{z}{\delta_{\mathrm{Skin}}}\right) \cdot \begin{pmatrix} -\frac{\sqrt{2}\,\tau}{\pi\,\delta_{\mathrm{Skin}}} \cdot \cos\left(\pi\,\frac{x}{\tau} + \omega_{\mathrm{s}}\,t - \frac{z}{\delta_{\mathrm{Skin}}} + \frac{\pi}{4}\right) \\ 0 \\ \sin\left(\pi\,\frac{x}{\tau} + \omega_{\mathrm{s}}\,t - \frac{z}{\delta_{\mathrm{Skin}}}\right) \end{pmatrix} . \qquad (10)$$

Furthermore, the current density distribution in the secondary j_2 can be found with

$$\vec{j} = {}^{1}/_{\mu_2}\, \nabla \times \vec{B} \qquad (11)$$

as

$$\vec{j_2} = \frac{\hat{B}_{\mathrm{g}}}{\mu_2} \cdot \exp\left(-\frac{z}{\delta_{\mathrm{Skin}}}\right) \left(\frac{2\,\tau}{\delta_{\mathrm{Skin}}^2\,\pi} \cdot \sin\left(\pi\,\frac{x}{\tau} + \omega_{\mathrm{s}}\,t - \frac{z}{\delta_{\mathrm{Skin}}}\right) + \frac{\pi}{\tau} \cdot \cos\left(\pi\,\frac{x}{\tau} + \omega_{\mathrm{s}}\,t - \frac{z}{\delta_{\mathrm{Skin}}}\right)\right) \cdot \begin{pmatrix} 0 \\ -1 \\ 0 \end{pmatrix} ; \qquad (12)$$

which, using (6) again yields

$$\vec{j_2} \approx \frac{\hat{B}_{\mathrm{g}}}{\mu_2} \frac{2\,\tau}{\delta_{\mathrm{Skin}}^2\,\pi} \cdot \exp\left(-\frac{z}{\delta_{\mathrm{Skin}}}\right) \cdot \sin\left(\pi\,\frac{x}{\tau} + \omega_{\mathrm{s}}\,t - \frac{z}{\delta_{\mathrm{Skin}}}\right) \cdot \begin{pmatrix} 0 \\ -1 \\ 0 \end{pmatrix} . \qquad (13)$$

2.1 *Lorentz Force Density*

Following the derivation of the flux density B_2 and the induced current density j_2, this section analyses the longitudinal (thrust or drag) and normal (lift) components of the Lorentz force.

The volumetric Lorentz force density

$$\vec{f} = \vec{j_2} \times \vec{B_2}, \qquad (14)$$

yields together with (10) and (13)

$$\vec{f} = -\frac{\hat{B}_{\mathrm{g}}^{\,2}}{\mu_2} \cdot \exp\left(-\frac{2\,z}{\delta_{\mathrm{Skin}}}\right) \frac{2\,\tau}{\delta_{\mathrm{Skin}}^2\,\pi} \cdot \sin\left(\pi\,\frac{x}{\tau} + \omega_{\mathrm{s}}\,t - \frac{z}{\delta_{\mathrm{Skin}}}\right) \cdot \begin{pmatrix} \sin\left(\pi\,\frac{x}{\tau} + \omega_{\mathrm{s}}\,t - \frac{z}{\delta_{\mathrm{Skin}}}\right) \\ 0 \\ \frac{\sqrt{2}\,\tau}{\delta_{\mathrm{Skin}}\,\pi} \cdot \cos\left(\pi\,\frac{x}{\tau} + \omega_{\mathrm{s}}\,t - \frac{z}{\delta_{\mathrm{Skin}}} + \frac{\pi}{4}\right) \end{pmatrix} . \qquad (15)$$

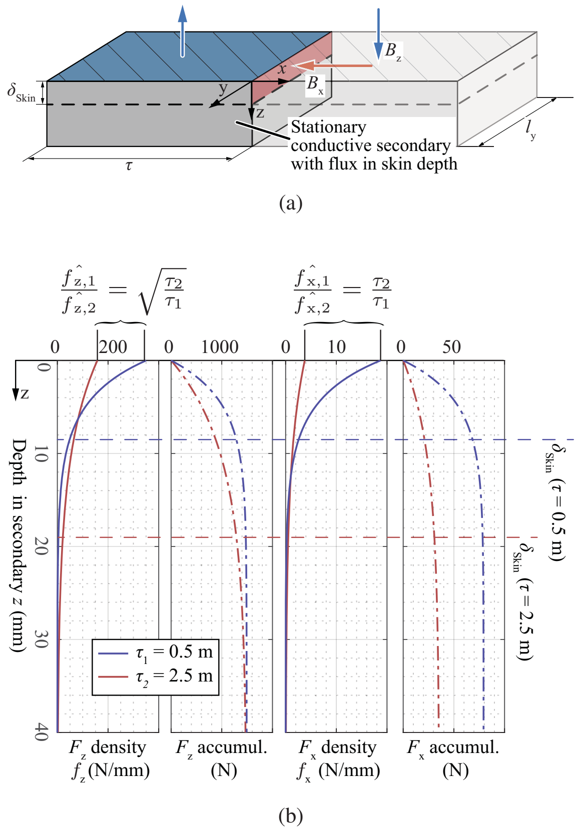

Fig. 3: (a) Illustration of flux conservation in the secondary. (b) Lift and drag force and their densities illustrated for a typical operation point of an EDS system and speed of 100 m/s for two different pole pitch values. While the peak value of drag force density is inversely proportional to pole pitch, the peak value of the lift force density is inversely proportional to the square root of the pole pitch. Therefore, an increased pole pitch reduces the drag coefficient significantly.

A surface force density σ, which is the force per magnetic interaction area A_{m} in the x-y plane (cf. Fig. 2), follows as

$$\sigma = \int_0^\infty f_x \mathrm{d}z \,. \qquad (16)$$

The average surface force density, which can be directly applied to an initial dimensioning of an EDS system follows as

$$\bar{\sigma} = \begin{pmatrix} \bar{\sigma}_{\mathrm{x}} \\ \bar{\sigma}_{\mathrm{y}} \\ \bar{\sigma}_{\mathrm{z}} \end{pmatrix} = \begin{pmatrix} -\frac{\hat{B}_{\mathrm{g}}^2\,\tau}{2\,\mu_2\,\delta_{\mathrm{Skin}}\,\pi} \\ 0 \\ \frac{\hat{B}_{\mathrm{g}}^2\,\tau^2}{2\,\mu_2\,\delta_{\mathrm{Skin}}^2\,\pi^2} \end{pmatrix} . \qquad (17)$$

Rewriting (17) with (2) and (8), the ratio $c_{\mathrm{D}} = \bar{\sigma}_{\mathrm{x}}/\bar{\sigma}_{\mathrm{z}} = F_{\mathrm{x}}/F_{\mathrm{z}}$, which describes the relation between longitudinal force F_{x} and lift force F_{z} can be derived as

$$c_{\mathrm{D}} = \pi\,\frac{\delta_{\mathrm{Skin}}}{\tau} = \sqrt{\frac{2\,\pi}{\tau\,\kappa_2\,\mu_2\,v_{\mathrm{s}}}} \,. \qquad (18)$$

In the case of a PM array fixed to the pod's bottom, c_{D} is the drag-to-lift ratio, or as it will be called in the rest of this paper, the drag coefficient.

The specific power demand per lift force follows as

$$c_{\mathrm{P}} = c_{\mathrm{D}}\, v_{\mathrm{s}} = \sqrt{\frac{2\,\pi\, v_{\mathrm{s}}}{\tau\, \kappa_2\, \mu_2}} \ . \tag{19}$$

Consequently, the instantaneous power demand P_{travel} of the system can be calculated as

$$P_{\mathrm{travel}} = m \cdot g \cdot \underbrace{c_{\mathrm{D}} \cdot v_{\mathrm{s}}}_{c_{\mathrm{P}}} \ , \tag{20}$$

where m is the total vehicle mass and g is the gravity. Hence, the propulsion system must be able to supply the required amount of power P_{travel} to maintain a constant speed.

2.2 *Interpretation of Drag Coefficient Scaling*

The above derived drag coefficient equation (18) shows directly how the losses of an EDS system scale with the secondary conductivity κ_2, the pole pitch τ and the slip speed v_{s}. Further results in this work are for an aluminium secondary with $\kappa_2 = 35\,\mathrm{MS/m}$, which is in accordance to most research projects in the field of EDS high-speed transportation (e.g. [7]). However, according to the scaling law (18), introducing a copper secondary would reduce the losses, regardless of the practical realization of the levitator, by a factor of $\sqrt{\kappa_{\mathrm{Al}}/\kappa_{\mathrm{Cu}}} = 0.78$ or 22%.

In order to illustrate the effect of the pole pitch τ on the drag coefficient, the cause for build-up drag and lift force shall be analysed briefly. Clearly, the drag F_{x} is developed by the vertical component of the flux B_{z} and the current (density) flowing in the secondary j_2. On the other hand, the lift force F_{z} is developed by the horizontal flux component in the secondary B_{x} and the current (density) flowing in the secondary j_2. Due to the skin effect and the law of magnetic flux conservation, illustrated for this specific case in Fig. 3a, the relation between flux in horizontal direction and vertical direction is

$$B_{\mathrm{x}} \cdot \delta_{\mathrm{Skin}} \sim B_{\mathrm{z}} \cdot \tau \ . \tag{21}$$

Since the skin depth (cf. (8)) scales with (2) as $\delta_{\mathrm{Skin}} \sim 1/\sqrt{\tau}$, the influence of the pole pitch τ on the drag coefficient must scale as

$$c_{\mathrm{D}} = \frac{F_{\mathrm{x}}}{F_{\mathrm{z}}} \sim \frac{\delta_{\mathrm{Skin}} \cdot j_2}{\tau \cdot j_2} \sim \frac{1}{\sqrt{\tau}} \ . \tag{22}$$

Moreover, Fig. 3b shows for two pole pitch values how lift force and drag develop over the depth in the secondary. One can see that most of the force (and secondary losses due to drag) is generated in the skin depth. While the peak value of drag force (F_{x}) density is proportional to $F_{\mathrm{x}} \sim 1/\tau$, the peak value of the lift force (F_{z}) density is proportional to $F_{\mathrm{x}} \sim 1/\sqrt{\tau}$.

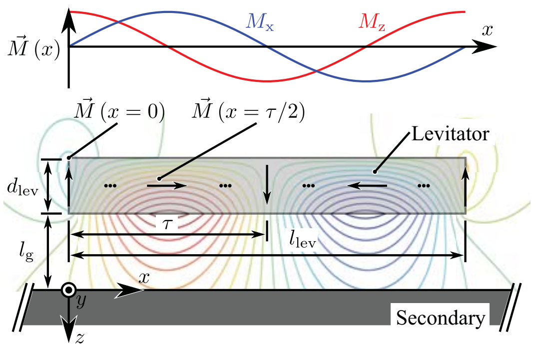

(a)

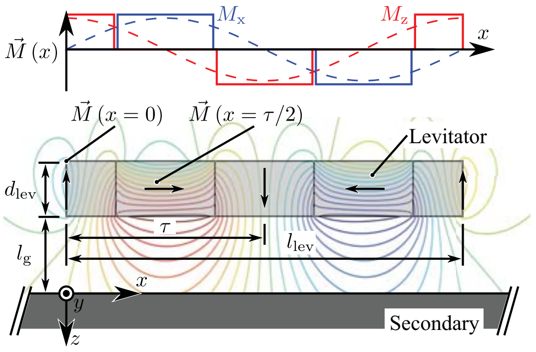

(b)

Fig. 4: (a) Magnetization pattern and magnetic field lines of an ideal Halbach magnet with continuous magnetization; and (b) a practical Halbach array consisting of discrete magnets, with an incremental angle of magnetization φ_{im} of 90°.

Table 1 Dimensions and material properties used for simulations.

Parameter		Value/range	Unit
Pole pair number	p	1...6	(1)
Pole pitch	τ	0.25...3.50	(m)
Levitator height	d_{lev}	0.2	(m)
Speed	v_1	25...350	(m/s)
Magnet coercitivity	H_{cb}	890	(kA/m)
Sec. conductivity	κ_2	35	(MS/m)
Magnet permeability	μ_1	1 μ_0	(Vs/Am)
Sec. permeability	μ_2	1 μ_0	(Vs/Am)

3 Verification of the Scaling Laws: Ideal and Practical EDS Systems

2D FEM simulations are used in this section, first for the verification of the analytically derived scaling laws; and then, for the quantification of effects occurring in practical EDS systems. The first analysed effect is the finite length of the PM arrangement, which results in entry and exit effects. Those will be referred to as edge effects in the following. Secondly, the effect of higher-order magnetic field harmonics, originating from the realization of the primary as Halbach array will be studied.

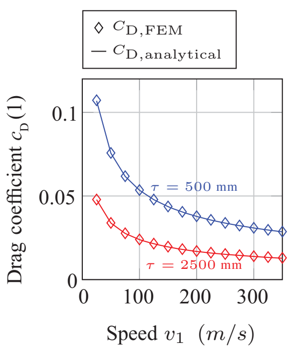

(a)

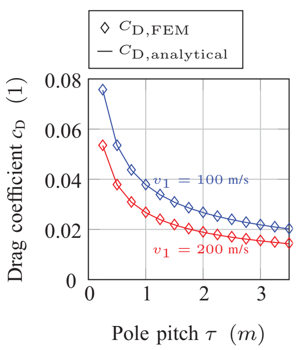

(b)

Fig. 5: The drag coefficient c_{D} over speed v_1 (a), and over pole pitch τ (b); calculated both analytically and with FEM. An infinitely long levitator with ideal Halbach magnetization is assumed.

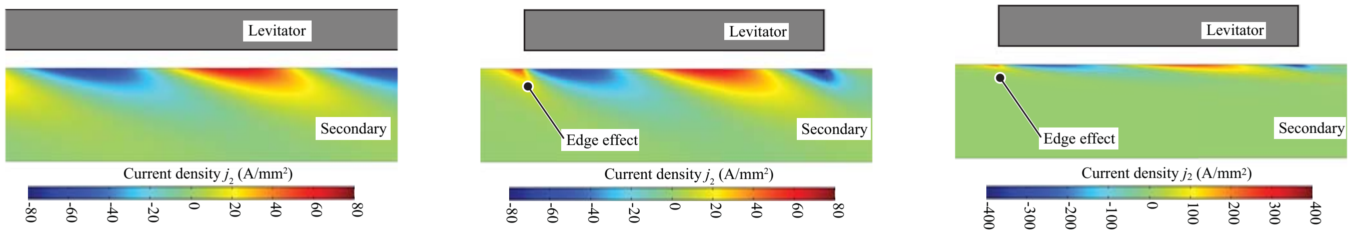

(a) (b) (c)

Fig. 6: (a) The induced current density in the secondary for an infinitely long magnet with continuous magnetization moving at $v_1 = 25$ m/s, (b) a finite magnet with pole pair number $p = 1$ moving at $v_1 = 25$ m/s showing the edge effects of the induced currents and (c) the same finite magnet moving at $v_1 = 350$ m/s illustrating the effect of high speeds on the skin depth of the induced current.

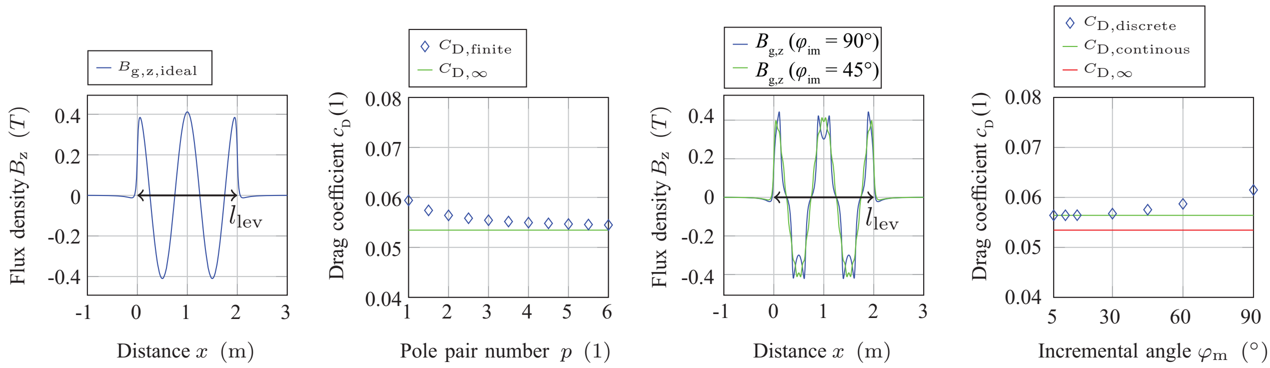

(a) (b) (c) (d)

Fig. 7: (a) Air gap flux density without interaction of the secondary for a finite-length magnet with pole pitch $\tau = 0.5$ m, pole pair number $p = 2$ and ideal Halbach magnetization; and (b) the drag coefficient c_D for a finite-length levitator and different pole pair numbers, for a speed of $v_1 = 100$ m/s. (c) The air gap flux density B_z without eddy current reaction, for a finite-length levitator with pole pitch $\tau = 0.5$ m and pole pair number $p = 2$, consisting of discretely magnetized magnets. (d) The drag coefficient c_D for a finite-length levitator with varying incremental angles of magnetization, for a speed of $v_1 = 100$ m/s.

In the following, the drag coefficient c_D is used to assess the effects of levitator imperfections. Table 1 lists the dimensions and material properties used for the FEM calculations.

3.1 *Infinitely Long, Ideally Magnetized Halbach Array*

An infinitely long magnet with ideal, sinusoidal Halbach magnetization is used in a first step to verify the scaling law. Fig. 4a shows the magnet and the secondary. The magnetization M of the magnet is

$$\vec{M}(x) = \begin{bmatrix} M_x(x) \\ M_z(x) \end{bmatrix} = \begin{bmatrix} M_0 \cdot \sin(x/\tau \cdot \pi) \\ M_0 \cdot \cos(x/\tau \cdot \pi) \end{bmatrix}, \tag{23}$$

with x being the position in x direction and M_0 the amplitude of the magnetization. The overall length of the levitator (consisting of an array of magnets with discrete magnetization or one sinusoidally magnetized magnet) is

$$l_{lev} = 2 \cdot p \cdot \tau, \tag{24}$$

where p is the number of pole pairs. The longitudinal boundaries of the model are defined as

$$\vec{A}(x = 0) = \vec{A}(x = l_{lev}) \tag{25}$$

with $\vec{A}$ being the magnetic vector potential. This corresponds to an infinitely long levitator since the magnetic vector potentials at both ends of the levitator are equal.

Fig. 5a and Fig. 5b show the analytically calculated drag coefficient and FEM simulation results for selected pole pitches and speeds. The derived scaling law and 2D FEM results agree well.

3.2 *Finite-Length, Ideally Magnetized Halbach Array*

An ideally magnetized levitator, cf. (23), with finite length is used to analyse the impact of longitudinal end effects on the levitator performance. This phenomenon is well known, described for linear induction machines and decreases the machine's performance due to exiting eddy currents, which do not longer contribute to thrust generation [24], p. 72. Similarly, for a levitator, finite length results in an increased drag coefficient. Fig. 6a shows the induced current density in the rail as an outcome of a 2D FEM simulation for a levitator with infinite length, while Fig. 6b shows the induced current density for a levitator with finite length. In Fig. 6a, the distribution of induced currents is homogeneous and shows a characteristic wave pattern. The distribution of eddy current fields in an EDS system with finite length shows inhomogeneities at the ends of the levitator, which is denoted as edge effect in Fig. 6b. For illustrative purposes, Fig. 6a and Fig. 6b are given for low speed ($v_1 = 25$ m/s) and hence, for a larger skin depth. Fig. 6c illustrates the field distribution of the system cruising at high speed ($v_1 = 350\,\mathrm{m/s}$).

For stating the quantitative effect of finite magnet length, Fig. 7a shows the z-component of the air gap field $B_{\mathrm{g,z}}$ for a levitator with $p = 2$ and $\tau = 0.5\,\mathrm{m}$. It shall be denoted that this is only the field of the magnet as defined in (1), without the eddy current reaction. The ends of the levitator lead to a steep slope of the field in the air gap.

Fig. 7b quantifies the end effect by comparing the drag coefficients $c_{\mathrm{D,finite}}$ for finite-length levitators with pole pitch $\tau = 0.5\,\mathrm{m}$ and different pole pair numbers p, moving at $v_1 = 100\,\mathrm{m/s}$. As expected, a performance degradation is seen, especially with lower pole pair numbers. Nevertheless, the increase of the $c_{\mathrm{D,finite}}$ is limited to 15%, and approaches the ideal value $c_{\mathrm{D},\infty}$ for a higher number of pole pairs.

3.3 *Finite-Length, Segmented Halbach Levitator*

Practical Halbach arrays are often assembled using discrete magnets, each with a uniform direction of magnetization. The angle between the magnetization directions of neighbouring magnets is denoted here with φ_{im}. Fig. 4b shows a Halbach array with $\varphi_{\mathrm{im}} = 90°$. Fig. 7c shows the z-component of the air gap field $B_{\mathrm{g,z}}$ for a levitator with $p = 2$ and $\tau = 0.5\,\mathrm{m}$ for $\varphi_{\mathrm{im}} = 90°$ and $\varphi_{\mathrm{im}} = 45°$.

The discrete magnetization leads to an additional distortion of the air gap field and increases the drag coefficient. The amount of field distortion and the drag coefficient are inversely proportional to φ_{im} as shown in Fig. 7d. Smaller φ_{im} values constitute to a better approximation of the continuously magnetized levitator. This example shows that a levitator with a discretization angle of $\varphi_{\mathrm{im}} = 90°$ features a drag coefficient c_{D} that is $\approx 9\%$ higher compared to a continuously magnetized levitator. However, a reduction of the discretization angle below $\varphi_{\mathrm{im}} < 15°$ does not reduce of the drag coefficient significantly.

3.4 *Effects of Finite Levitator Width and Length*

For the example design given in Table 2, end and edge effects due to the EDS levitator's finite length and width as well as the discretization of its Halbach array ($\varphi_{\mathrm{im}} = 15^{\mathrm{o}}$) are analysed. The simulation is conducted in 3D with a numeric method based on [25–27]. Fig. 8a illustrates the magnetic field on the surface of the aluminium rail for a speed of $v_1 = 100\,\mathrm{m/s}$. One can identify a certain distortion due to finite length and width of the levitator. However, comparing the scaling law to the 3D simulation in Fig. 8b shows that the deviation is minor. The error of the scaling law was found to be $< 10\%$ for interesting speeds of $v_1 > 100\,\mathrm{m/s}$.

This clearly demonstrates that the analytical scaling laws are a valid tool for the initial design of practical systems, even though they have been derived assuming an ideal levitator.

4 Case Study: Levitator for the *Hyperloop* Competition

In order to illustrate the application of EDS in high-speed transportation further, an example levitation system in accordance to the specifications of the *Hyperloop* student competition [28] is given in this section. The levitation system is composed of two levitators, designed to float on the pair of flat aluminium surfaces running parallel to each other at the bottom of the evacuated tube. Each levitator is 2 m long and weights $m_{\mathrm{lev}} = 30$ kg. The system has a pay-load capacity of up to $m_{\mathrm{p}} = 250$ kg, while guaranteeing an air gap above 10 mm for speeds exceeding 25 m/s (90 km/h). Based on results in Sec. 3.3, the incremental angle of magnetization is set to $\varphi_{\mathrm{im}} = 15°$. The magnet discretization results in only 7 differently magnetized blocks of magnets (0^{o}, 15^{o}, 30^{o}, 45^{o}, 60^{o}, 75^{o}, 90^{o}) with using the symmetry properties of the arrangement. With the chosen pole pitch $\tau = 500\,\mathrm{mm}$, the levitator's discrete magnets can be realized as blocks of $\tau/24 = 20.8\,\mathrm{mm}$ length (in x-direction), $w_{\mathrm{lev}} = 120\,\mathrm{mm}$ width (in y-direction) and $h_{\mathrm{lev}} = 16\,\mathrm{mm}$ height (in z-direction). Further dimensions of the proposed design are summarized in Table 2.

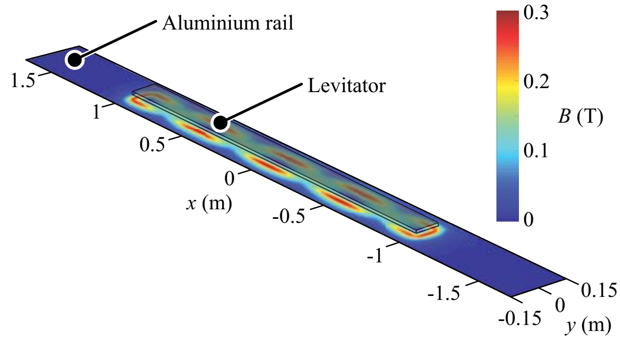

(a)

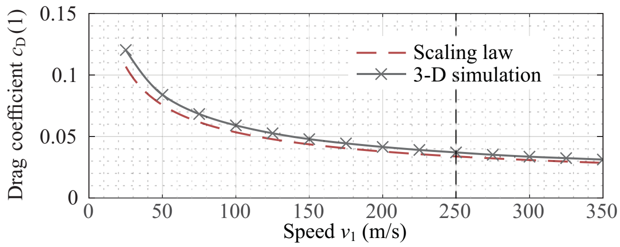

(b)

Fig. 8: (a) 3D simulation result, illustrating the magnetic field on the aluminium rail due to one levitator according to Table 2 at a speed of $v_1 = 100\,\mathrm{m/s}$. (b) Comparison of the drag coefficient predicted by the scaling law and 3D simulation result for the levitator according to Table 2. For speeds $v_1 > 100\,\mathrm{m/s}$ the scaling law deviates $< 10\%$ from the 3D simulation.

Table 2 Dimensions of the example system.

Parameter	Symbol	Value	Unit
No. of levitators		2	(1)
Levitator length	l_{lev}	2	(m)
Levitator width	w_{lev}	0.12	(m)
Levitator height	h_{lev}	0.016	(m)
Pole pitch	τ	0.5	(m)
Incremental magnet. angle	φ_{im}	15	(°)
Levitator weight	m_{lev}	30	(kg)
Payload	m_{p}	250	(kg)

4.1 *Steady State Air Gap and 1-D Dynamics of an EDS System*

Fig. 9 shows the lift force of one levitator and the gravitational force $(m_{\mathrm{p}}/2 + m_{\mathrm{lev}})\,g$ of the mass, which is lifted by one levitator. The force equilibrium

$$F_{\mathrm{z,L}}\left(l_{\mathrm{g,S}}, v_1\right) = F_{\mathrm{z,g}} = \left(m_{\mathrm{p}}/2 + m_{\mathrm{lev}}\right) g \tag{26}$$

determines the speed dependent, steady-state air gap $l_{\mathrm{g,S}}$. Fig. 9 shows this for the limits of the operational range (25 m/s and

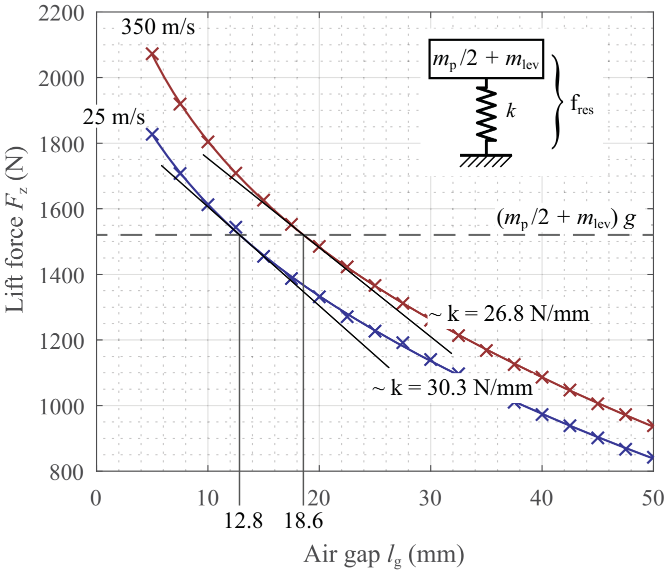

Fig. 9: Lift and gravitational forces acting on the levitation system for different air gaps and velocities, and stable air gap defined by the intersection with the gravitational force for the given payload. Tangents on the steady-state operating points show the stiffness of the EDS system.

$350\ \mathrm{m/s}$). The steady-state air gap stays within $12.8\ \mathrm{mm} \leq l_{g,S} \leq 18.6\ \mathrm{mm}$.

As an extended vehicle stability analysis of an electrodynamically suspended pod is beyond the scope of this paper and task of further research, only a one-dimensional analysis of the resonance frequency is conducted, where a vertical displacement of the pod is considered. Tangent lines at the steady state levitation points in Fig. 9 show the stiffness of the proposed levitation system. As a displacement of the pod in direction of a decreased air gap causes an increase in lift force for all air gap positions, it can be concluded that the system is stable for small excitations and with regard to the considered displacement. With stiffness k and the pod's mass m, the (undamped) mechanical resonance frequency for vertical oscillations is

$$f_{\mathrm{res}} = \frac{1}{2\pi}\sqrt{\frac{k(v_1)}{m}} \approx 0.07\ \mathrm{Hz} \qquad (27)$$

for all operating conditions. This rather low frequency is well suited for active damping systems, as it shall be possible to design either electromagnetic or mechanical (e.g. by using compressed gas, which may already be on board and utilized for propulsion) active damping systems that feature a bandwidth well above $f_{\mathrm{res}} \approx 0.07$ Hz.

4.2 Considerations on the Achievable Range

In the following, the maximum range of the electrodynamically levitated high-speed pod shall be briefly discussed. Both the propulsion system and the energy storage systems are assumed to be on the pod, which is in accordance to [28]. It results in a very simple track structure with just flat conductors and no energized parts.

According to the results depicted in Fig. 8b, a drag coefficient of $c_{\mathrm{D}} = 0.04$ and speed of $250\ \mathrm{m/s}$ (approximately $900\ \mathrm{km/h}$ or 560 mph) is assumed. Therefore, the power required to overcome the drag of the levitation system and to maintain this constant speed is $P_{\mathrm{travel}} = 30$ kW. For the sake of simplicity, it is assumed at a first step that the total mass of the energy storage m_{bat} accounts for one third of the total vehicle mass m_{tot}. At this point losses of the energy storage and the propulsion system are neglected. The required power density of the energy storage P'_{bat} can then be calculated as

$$P'_{\mathrm{bat}} = \frac{P_{\mathrm{travel}}}{m_{\mathrm{bat}}} = 3 \cdot g \cdot c_{\mathrm{D}} \cdot v_1 = 0.29\ \mathrm{kW/kg}. \qquad (28)$$

This is well below the power density of batteries used in commercial electric vehicles [29], eg. *Chevrolet Volt*: $P'_{\mathrm{bat}} \approx 0.65\ \mathrm{kW/kg}$ [30]. Using the energy density $W'_{\mathrm{bat}} \approx 0.1\ \mathrm{kWh/kg}$ of the aforementioned lithium-ion battery system, the reachable range x_{range} is

$$x_{\mathrm{range}} = \frac{W'_{\mathrm{bat}}}{3 \cdot g \cdot c_{\mathrm{D}}} \approx 300\ \mathrm{km}. \qquad (29)$$

The range can be extended further by an energy storage with higher energy density, battery replacement stations, or (wireless) charging along the track. Alternatively, the energy storage and propulsion can be removed from the pod entirely by using an energized track that acts as the stator of a linear machine, whose mover is attached to the pod [7].

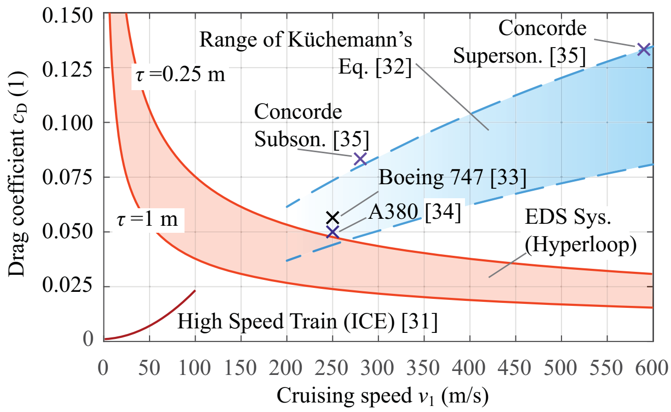

Fig. 10: Comparison of the drag coefficient c_{D} of an electrodynamically suspended vehicle with that of other high-speed ground and air transportation systems. For the electrodynamically suspended vehicle an ideally evacuated tube was assumed and henceforth, the air friction resistance is neglected. At high speeds ($> 200\ \mathrm{m/s}$) the EDS system shows lower drag resistance compared to commercial aircraft, while it can be operated noticeably above the operating range of conventional high-speed trains (ICE).

5 Comparison with Other Forms of High-Speed Transportation

In this section, an electrodynamically suspended vehicle is compared to other high-speed ground and air transportation systems. In order to achieve a simple comparison, several aspects such as their related propulsion/traction methods and their efficiencies or environmental impact are left out. Moreover, the vehicle is assumed to travel in a tube, which is completely air-evacuated (as e.g. proposed for the *Hyperloop*) and the drag coefficient of the EDS system c_{D} is selected as the sole performance metric. Fig. 10 depicts this comparison.

State-of-the-art high-speed ground transportation is represented in Fig. 10 by the German *Inter City Express* (ICE). The rolling resistance and the air-friction resistance of an ICE with 14 coaches and and a mass of 800 000 kg is calculated according to Sauthoff's equation [31], p. 40, up to 100 m/s. There is no literature for the rolling resistance of high-speed trains above this speed, since the high stresses in the mechanical suspension systems prevent increasing the speed further for regular passenger transportation. However, the rolling resistance of today's modern high-speed trains is much lower compared to the drag coefficient of an EDS system below $100\,\mathrm{m/s}$ ($360\,\mathrm{km/h}$ or 224 mph).

Nevertheless, the results turn in favour of the electrodynamically suspended vehicle when it is compared to state-of-the-art air transportation systems at speeds above $200\,\mathrm{m/s}$. Küchemann [32], p. 341, gives an expected range of cruising drag coefficients for various aircraft, which is plotted in blue in Fig. 10. The drag coefficients for cruising operation for a *Boeing 747* airplane [33], p. 20, an *Airbus A380* [34], p. 4, and *Concorde* supersonic plane [35], p. 26 broaden this picture. Hence, it can be concluded that an electromagnetically suspended vehicle (e.g. *Hyperloop* pod) can significantly reduce the power required to cruise at speeds exceeding $250\,\mathrm{m/s}$ compared to today's airplanes.

6 Conclusion

In this paper a simple, yet accurate analytical model for an electrodynamic suspension (EDS) system has been derived. Scaling laws (cf. (18) and (19)) are deducted from the model and give insight in the build up of the drag coefficient, which is drag per obtained lift force in an EDS system. The detailed modelling of the magnetic field source is omitted for the sake of simplicity, and a given magnetic field is assumed for the analysis in a first step. This enables the use of the presented method to evaluate various EDS systems with different excitations such as single-sided linear stators, rotating permanent magnets, and of course the most common and simplest variant, a static (fixed on a moving vehicle), linear Halbach array. According to the derived scaling law, the drag of the EDS system reduces with higher traveling speed, higher rail conductivity and longer pole pitch of the excitation system.

2D FEM models are first used to validate the analytical models. Afterwards, they are used to quantify the effects of practical design aspects, such as finite magnet length and the discrete realization of a Halbach array. Simulations verify the scaling law for the drag coefficient on practical EDS systems. An example levitator design is shown, which is in accordance to the specifications of the *Hyperloop* student competition. 3D simulations therefore considering finite levitator length and width as well as discretization of the EDS system's Halbach array ($\varphi_{\mathrm{im}} = 15^{\mathrm{o}}$) reveal that the error of the scaling law is minor ($< 10\%$) for higher speeds ($v_1 > 100\,\mathrm{m/s}$). Therefore, it can be concluded that the provided scaling law is sufficiently accurate for an initial design of an EDS system and for evaluating the feasibility of an application utilizing an EDS system. The study on the system realization concludes with analysing the resonance frequency of the suspension for an assumed displacement in vertical direction. For this mode it was calculated as $< 1\,\mathrm{Hz}$ for the design example. Stability analysis of the analysed concept, considering all degrees of freedom in displacement as well as considerations on the track guiding of the levitated vehicle shall be analysed in forthcoming publications.

Finally, comparing the drag coefficient of EDS systems to other forms of state-of-the-art high-speed ground and air transportation presents an interesting picture. Above the cruising speeds of modern subsonic airliners, an electrodynamically levitated vehicle in an evacuated tube (e.g. *Hyperloop*) has the potential of increasing the cruising-speed energy efficiency significantly. The drag due to the EDS system decreases with increasing traveling speed, while air friction of airliners increases with traveling speed.

Acknowledgment

Acknowledgment is given to Tibor Stolz who contributed to the 3D eddy current simulation in the course of his M.Sc. thesis.

7 References

1 M. Verne, *An Express of the Future*. The Floating Press, 1895.
2 R. H. Goddard, "Vacuum tube transportation system," US Patent 2 511 979, 1950.
3 R. Palacin, "Hyperloop, the electrification of mobility, and the future of rail travel," *IEEE Electrification Magazine*, vol. 4, no. 3, pp. 4–51, September 2016.
4 R. Janzen, "Transpod ultra-high-speed tube transportation: Dynamics of vehicles and infrastructure," *Procedia Engineering*, September 2017.
5 Y. Yang, H. Wang, M. Benedict, and D. Coleman, "Aerodynamic simulation of high-speed capsule in the hyperloop system," in *Proc. Conf. AIAA*, June 2017.
6 P. E. Ross, "Hyperloop: No pressure," *IEEE Spectrum*, vol. 53, no. 1, pp. 51–54, January 2016.
7 SpaceX. Hyperloop alpha. [Online]. Available: http://www.spacex.com/hyperloopalpha, accessed: October 2017.
8 R. F. Post and D. D. Ryutov, "The inductrack: a simpler approach to magnetic levitation," *IEEE Trans. Appl. Supercond.*, vol. 10, no. 1, pp. 901–904, March 2000.
9 Swissloop Team Website. (2017). [Online]. Available: http://www.swissloop.ch/, accessed: October 2017.
10 R. Knowles, "Dynamic circuit and fourier series methods for moment calculation in electrodynamic repulsive magnetic levitation systems," *IEEE Trans. Magn.*, vol. 18, no. 4, pp. 953–960, July 1982.
11 R. J. Hill, "Teaching electrodynamic levitation theory," *IEEE Trans. Educ.*, vol. 33, no. 4, pp. 346–354, November 1990.
12 W. Ko and C. Ham, "A novel approach to analyze the transient dynamics of an electrodynamics suspension Maglev," *IEEE Trans. Magn.*, vol. 43, no. 6, pp. 2603–2605, June 2007.
13 A. Najjar-Khodabakhsh and S. Vaez-Zadeh, "Analysis of passive suspension systems with flat and cylindrical structures," in *Proc. IET PEMD*, April 2008, pp. 553–556.
14 W. Jiangbo, L. Chunsheng, X. Wei, and Y. Baofeng, "Optimization design of linear halbach array for EDS maglev," in *Proc. IEEE VPPC*, September 2008, pp. 1–5.
15 Y. Junyou, Z. Meiwen, C. Jiefan, and W. Chengyuan, "Force analysis and test facility for permanent magnet levitation system," in *Proc. ICEMS*, vol. 2, August 2001, pp. 872–875 vol.2.
16 M. Carlstedt, K. W. nee Porzig, M. Ziolkowski, R. Schmidt, and H. Brauer, "Estimation of lorentz force from dimensional analysis: similarity solutions and scaling laws," *IEEE Trans. Magn.*, vol. 52, no. 8, pp. 1–13, August 2016.
17 Y. Chen and K. L. Zhang, "Calculation and analysis of the forces created by halbach permanent-magnet electrodynamic suspension," in *Applied Mechanics and Materials*, vol. 229. Trans Tech Publ, 2012, pp. 440–443.
18 S. Paul, W. Bomela, N. Paudel, and J. Z. Bird, "3-D eddy current torque modeling," *IEEE Trans. Magn.*, vol. 50, no. 2, pp. 905–908, February 2014.
19 K. Ogawa, Y. Horiuchi, and N. Fujii, "Calculation of electromagnetic forces for magnet wheels," *IEEE Trans. Magn.*, vol. 33, no. 2, pp. 2069–2072, March 1997.
20 J. H. Park and Y. S. Baek, "Design and analysis of a maglev planar transportation vehicle," *IEEE Trans. Magn.*, vol. 44, no. 7, pp. 1830–1836, July 2008.
21 K. Yoshida and S. Nonaka, "Levitation forces in single-sided linear induction motors for high-speed ground transport," *IEEE Trans. Magn.*, vol. 11, no. 6, pp. 1717–1719, November 1975.
22 A. A. Kuijpers, C. Nemlioglu, F. Sahin, A. Verdel, J. C. Compter, and E. A. Lomonova, "Force analysis of linear induction motor for magnetic levitation system," in *Proc. EPE-PEMC*, September 2010, pp. S3–17–S3–20.
23 M. Flankl, A. Tüysüz, and J. W. Kolar, "Analysis and power scaling of a single-sided linear induction machine for energy harvesting," in *Proc. IEEE IECON*, November 2015, pp. 835–842.
24 I. Boldea, *Linear Electric Machines, Drives, and MAGLEVs Handbook*. CRC Press, 2013.
25 D. Rodger, T. Karguler, and P. J. Leonard, "A formulation for 3D moving conductor eddy current problems," *IEEE Trans. Magn.*, vol. 25, no. 5, pp. 4147–4149, September 1989.
26 J. Bird and T. A. Lipo, "Calculating the forces created by an electrodynamic wheel using a 2-D steady-state finite-element method," *IEEE Trans. Magn.*, vol. 44, no. 3, pp. 365–372, March 2008.
27 N. Paudel, "Dynamic suspension modeling of an eddy-current device: an application to MAGLEV," Ph.D. dissertation, The University of North Carolina at Charlotte, 2012.
28 SpaceX. Spacex hyperloop pod competition ii. [Online]. Available: http://www.spacex.com/hyperloop, accessed: October 2017.
29 B. Scrosati, J. Garche, and W. Tillmetz, *Advances in Battery Technologies for Electric Vehicles*. Woodhead Publishing, 2015.
30 Ford. (2017, April) 2016 chevrolet volt battery system. [Online]. Available: https://media.gm.com/content/dam/Media/microsites/product /Volt_2016/doc/VOLT_BATTERY.pdf, accessed: October 2017.
31 A. Steimel, *Elektrische Triebfahrzeuge und ihre Energieversorgung (in German)*, 3rd ed. Deutscher Industrieverlag, 2014.
32 D. Küchemann, *The Aerodynamic Design of Aircraft*. McGraw-Hill Book Company, 1978.
33 E. Obert, *Aerodynamic Design of Transport Aircraft*. IOS Press under the imprint Delft University Press, 2009.
34 N. Cumpsty, *Jet Propulsion*. Cambridge University Press, 2003.
35 C. Orlebar, *The Concorde Story*. Osprey Publishing, 1997.